Nano Research

Open Access

Research Article

Se temperature drives coordination between liquid-intermedia-phase assisted crystallization and $NaSe_x$ assisted crystallization of $Cu_2ZnSn(S,Se)_4$ film

Chao Gao ✉, Yujiao Ma, Yang Liu, Yanxin Huo, Cong Song, Rui Zhang, Qing Zhou, Xinzhan Wang, Wei Yu ✉, and Zhiqiang Li ✉

College of Physics Science and Technology, National & Local Joint Engineering Laboratory for New Energy Opto-electronics Devices, Province-Ministry Co-construction Collaborative Innovation Center of Hebei Photovoltaic Technology, Hebei Key Laboratory of Photo-Electricity Information and Materials, Hebei University, Baoding 071002, China

Cite this article: *Nano Research*, **2025**, *18*, 94907791. https://doi.org/10.26599/NR.2025.94907791

ABSTRACT: Different crystallization mechanisms may co-exist during the crystallization of $Cu_2ZnSn(S,Se)_4$ (CZTSSe) film. To improve the properties of CZTSSe film, coordination between different crystallization mechanisms should be accomplished, which is challenging work. Herein, synergistical optimization of liquid-intermedia-phase assisted crystallization and $NaSe_x$ assisted crystallization of CZTSSe film is achieved by simply adjusting the Se temperature of selenization. On one hand, the S-to-Se substitution of the film can be delayed by decreasing the Se temperature. This can facilitate the formation of liquid-intermedia-phase, thereby improving the bulk crystallization of the CZTSSe film. On the other hand, the decreased Se temperature can optimize the properties of $NaSe_x$ flux by altering the reaction between Se and sodium source, thus improving the surficial crystallization of CZTSSe film. By regulating the above two crystallization mechanisms, the crystallinity, morphology and defect properties of CZTSSe film are improved simultaneously, which yields CZTSSe solar cells with the best efficiency of 12.3% (without anti-reflection coating). This paper reveals the complex mechanisms that how the Se source affects the crystallization of CZTSSe film, the results show the prospect of coordinating different crystallization mechanisms for high efficiency CZTSSe solar cell.

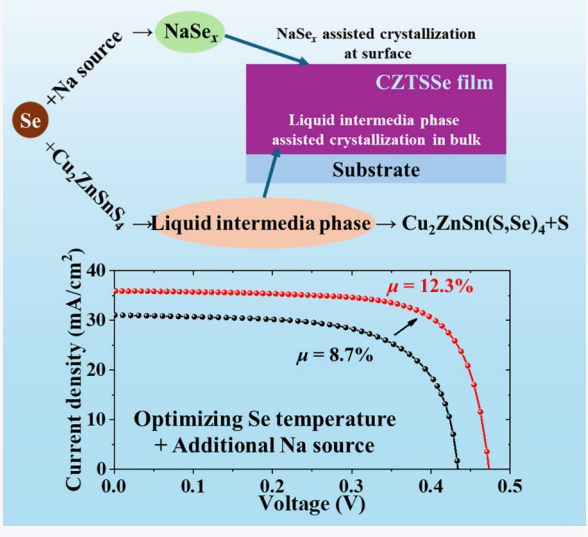

KEYWORDS: $Cu_2ZnSn(S,Se)_4$, crystallization mechanism, Se source temperature, solar cell

1 Introduction

The earth abundant $Cu_2ZnSn(S,Se)_4$ (CZTSSe) photovoltaic material has attracted the attentions of researchers in the past decades [1–7]. With their efforts, the best CZTSSe solar cell can reach the efficiency of 15.1% [8]. However, this efficiency record is much lower than the theoretical efficiency of CZTSSe solar cell. The main factor that limits the efficiency of CZTSSe solar cell is the low open circuit voltage (V_{OC}), which is believed caused by the serious recombination in the CZTSSe absorber layer [9–12].

Due to the multinary constitution of the material, CZTSSe exhibits complex defect properties (i.e., multiple intrinsic defects can be generated in CZTSSe). According to the first-principle calculation, some of the intrinsic defects in CZTSSe can act as deep level defects (e.g., Sn_{Zn}), which may cause the carrier recombination of the semiconductor [13–16]. Besides, poor crystallinities (e.g., fine-grain layers) are usually reported in real CZTSSe films, which may result in the massive generation of the lattice defects. Except that, the incomplete cation exchange during the formation of CZTSSe could promote the formation of the deep-level Sn_{Zn} defect [17].

Received: April 15, 2025; **Revised:** June 4, 2025
Accepted: July 13, 2025

✉Address correspondence to Chao Gao, cgao@hbu.edu.cn; Wei Yu, yuwei@hbu.edu.cn; Zhiqiang Li, lizhiqiang@hbu.edu.cn

These can deteriorate the defect problem of CZTSSe film, thus causing serious carrier recombination and large V_{OC}-deficit of the solar cell.

To optimize the defect properties of CZTSSe film, one can adjust the composition of the film (e.g., a Sn-poor composition may inhibit the formation of Sn_{Zn} defect in CZTSSe), or use alloying strategy (i.e., partly substitution of Cu/Zn/Sn with Ag/Cd/Ge, which can enhance the citation exchange, thus suppressing the formation of Sn_{Zn} defect) [13–21]. Except that, from the viewpoint of crystallization, the crystallinity and lattice defects of CZTSSe film are directly related to the crystallization of the film. To suppress the formation of lattice defects that caused by the poor crystallinity and improve the defect properties of the CZTSSe crystalline grains, it is necessary to optimize the crystallization of CZTSSe film [22–32].

In previous works, different crystallization mechanisms of CZTSSe film have been investigated. For example, obvious S-to-Se substitution of the film at high temperature (> 500 °C) may trigger the generation of liquid-intermedia-phase, thereby causing the liquid-intermedia-phase assisted crystallization. Such mechanism can greatly improve the bulk crystallization and decrease the band-tail energy of CZTSSe film [33, 34]. Except that, the reaction between selenium and sodium-contained matter (e.g., sodium lime glass) in selenization could result in the formation of liquid $NaSe_x$ flux on top of the film, thereby causing the $NaSe_x$ assisted crystallization. This mechanism mainly affects the surficial crystallization of CZTSSe film (specifically, $NaSe_x$ with suitable properties may influence the bulk crystallization by enhancing the elemental diffusion) [35]. During the crystallization of CZTSSe film, the different crystallization mechanisms may coexist and play their unique roles. If the different crystallization mechanisms can be coordinated, the crystallization and properties of CZTSSe film could be improved. Considering that both the S-to-Se substitution and formation of $NaSe_x$ flux are related to Se, it might be possible to regulate the above crystallization mechanisms by modifying the Se source.

In this paper, we propose to coordinate the liquid-intermedia-phase assisted crystallization and $NaSe_x$ assisted crystallization of CZTSSe film by modifying the temperature of Se source. By decreasing the Se temperature, the S-to-Se substitution of the film can be delayed to higher temperature. As a result, more liquid-intermedia-phase could be generated which can improve the bulk crystallization of the CZTSSe film (e.g., eliminating the fine-grain layer). Meanwhile, the decreased Se temperature can yield $NaSe_x$ flux with suitable properties by altering the reaction between Se and sodium lime glass (SLG) substrate, thus improving the surficial crystallization of the CZTSSe film (e.g., facilitating the formation of shallow acceptor, suppressing the deep level Sn_{Zn} defect). Consequently, both the crystallinity and defect properties of CZTSSe film are improved by optimizing the Se temperature. Moreover, we have tried to enhance the $NaSe_x$ assisted crystallization by adding Na_2S source for selenization. Such a strategy can eliminate the bi-layer crystallization and optimize the defect properties of CZTSSe film. By optimizing the crystallization of CZTSSe film, the efficiency of CZTSSe solar cell is improved to 12.3% (without using alloying strategy for the CZTSSe layer). This paper reveals the relationships between Se source and the different crystallization mechanisms of CZTSSe film. The results would pave the way for the comprehensive optimization on crystallization of CZTSSe film.

2 Experimental details

2.1 Preparation processes of CZTSSe films and solar cells

CZTSSe films were prepared using a dimethyl sulfoxide (DMSO) based solution method, which follows the methods in previous publications [33, 36, 37]. Firstly, the precursor solution was prepared by dissolving 2.3 mmol of $Cu(CH_3COO)_2{\cdot}H_2O$, 1.7 mmol of $SnCl_2{\cdot}2H_2O$, 1.6 mmol of $ZnCl_2$, and 5.5 mmol of $CS(NH_2)_2$ in 2 mL of DMSO solvent. Then, the precursor film was prepared by spin-coating the precursor solution (3500 r/min for 35 s) and drying the coating (350 °C for 2 min) on SLG/Mo substrate (the spin-coating and drying processes were successively repeated for 7 times in a nitrogen filled glove box). After that the precursor films were pre-annealed at 350 °C for 30 min in nitrogen atmosphere.

A graphite box was used to selenize the precursor film. To adjust the Se temperature, ceramic crucible and ceramic slice were placed below the Se pellets. Since the crucible parts were low thermal conductive, the temperature of the Se source could be decreased by isolating from the high thermal conductive graphite. To verify whether the crucible parts can decrease the Se temperature, a thermal imaging was tested for a hot plate on which ceramic parts were placed. The result (Fig. S1 in the Electronic Supplementary Material (ESM)) proved that the surface temperature can be decreased by placing ceramic crucible and ceramic slice on the hot plate. Consequently, the different Se temperatures may result in different Se partial pressures in selenization processes. The sketch for the selenization of CZTSSe films is shown in Fig. 1(a). Before the process, nitrogen with a pressure of 250 Torr was filled to provide protecting atmosphere, then the temperature was ramped up following the profile in Fig. S2 in the ESM. The CZTSSe film that selenized by placing Se pellets directly on graphite box was named as Se-WO. By placing a ceramic crucible below the Se pellets, Se-CC film was prepared. The Se-CCF film was obtained by putting a ceramic slice below the ceramic crucible which contains Se pellets. To investigate the crystallization of CZTSSe films, half-selenized films were prepared by terminating the heating process at different temperatures of the temperature profile (see Fig. S2 in the ESM). For selenization with additional Na_2S source, quartz glass slide loaded with 1 mg of Na_2S (0.5 g of Na_2S was first dissolved in 50 mL of pure water, then 100 μL of solution was dropped and dried on the quartz glass slide) was placed in the graphite box. The other details were the same as the selenization without Na_2S source. Besides, to verify whether $NaSe_x$ can be deposited on the film, simulated selenizations were implemented by replacing the CZTSSe film with quartz glass slide.

The solar cells with the structure of Mo/CZTSSe/CdS/i-ZnO/ITO/Ni/Al were fabricated (without anti-reflection coatings). For solar cell fabrication, the CdS buffer layer (~ 50 nm) was deposited by chemical bath deposition, the i-ZnO (~ 50 nm) layer and ITO (~ 200 nm) layer were deposited by sputtering, and the Ni/Al metal grids were deposited by evaporation. After the fabrication, the solar cell was divided into small pieces with an area of 0.25 cm^2 (the mask area is 0.2 cm^2).

2.2 Characterization methods

The X-ray diffraction (XRD) patterns and the Raman spectra of the films were measured by Bruker D8 Advance X-ray diffractometer and JY LabRAM HR Raman spectrometer (with 532 nm laser). The morphologies and compositions of the films were characterized by

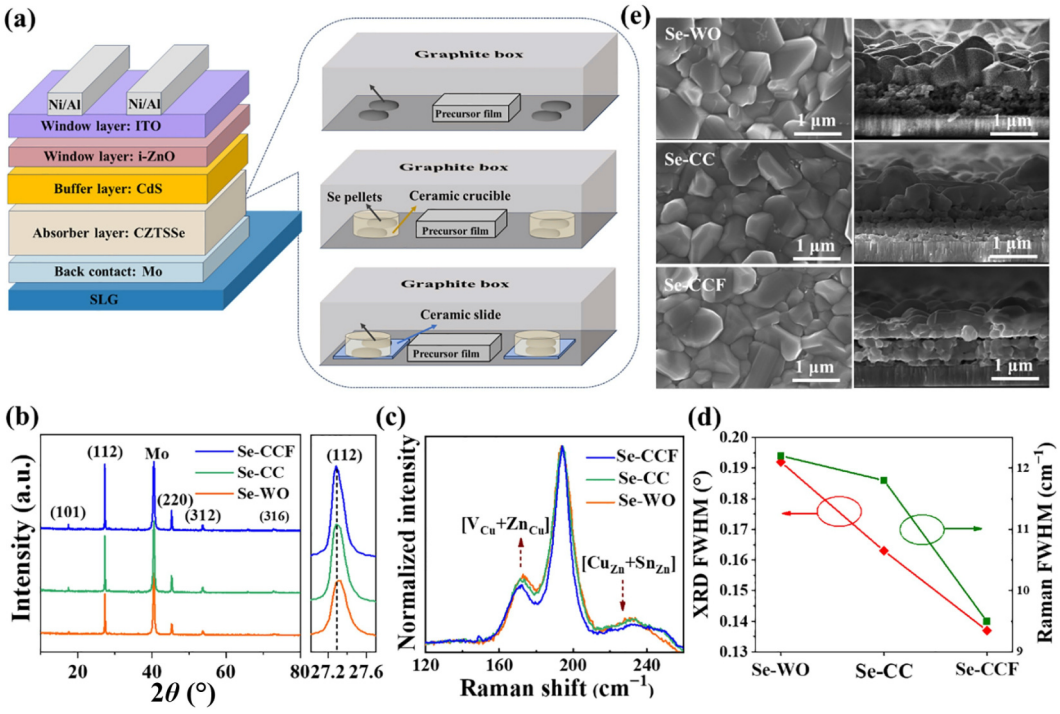

Figure 1 (a) Sketch for the preparation of CZTSSe films with different Se temperatures. (b) and (c) Raman spectra and XRD patterns of the CZTSSe film. (d) FWHM of the (112) diffraction peaks and Raman peaks at 197 cm^{-1}. (e) SEM images of the CZTSSe films.

Nova nanoSEM450 scanning electron microscopy (SEM). The X-ray photoelectron spectra (XPS) of the films were obtained by Escalab 250Xi X-ray photoelectron spectroscopy (during the whole process of the measurement, the neutralizer of the XPS setup was opened to neutralize the charges that exist on the surface of the sample). The current–voltage (*I*–*V*) and capacity–voltage (*C*–*V*) curves of the solar cells were tested by Agilent B1500A semiconductor device analyzer at room temperature (AM1.5G irradiation was used for the *I*–*V* test). The external quantum efficiencies (EQE) curves of the solar cells were acquired by QTesT 1000ADX setup. The admittance spectra of the solar cells were tested by Keysight E4980A LCR meter. The electrochemical impedance spectroscopy (EIS) and Suns-V_{OC} tests of the solar cells were measured by PGSTAT302N electrochemical workstation WCT-120 silicon wafer lifetime tester, respectively.

3 Results and discussions

3.1 Effect of Se temperature on properties of CZTSSe film and solar cell

Figure 1 shows the XRD patterns, Raman spectra, and SEM images of the selenized films (after the whole selenization processes, denoted as 530/20 in Fig. S2 in the ESM). The XRD and Raman results (Figs. 1(b) and 1(c)) prove that all the films are mainly constituted by CZTSSe (the shift of the (112) diffraction peak could be attributed to the different Se/(S+Se) ratios of the CZTSSe film). Moreover, both the full width at half maxima (FWHM) of the (112) diffraction peaks and the Raman peaks (at 197 cm^{-1}) reduce as the decrease of Se temperature (Fig. 1(d), Table S1 in the ESM), indicating that the decreased Se temperature can improve the crystallinity of the CZTSSe film. Considering that the 532 nm light source for Raman measurement is mainly absorbed by the surficial region of CZTSSe film, the Raman characterizations could mainly reflect the surficial properties of CZTSSe film. Thus, the varied FWHM of Raman peaks reveal that the decreased Se temperature could improve the surficial crystallinity of CZTSSe film (the comparable grain sizes of the films in Fig. 1(e) indicates that the varied FWHM are not caused by the different grain sizes but should be caused by the different concentrations of lattice defects in the crystalline grains). Besides, SEM images show that fine-grain layers remain at the bottom of Se-WO and Se-CC films. However, the fine-grain layer is eliminated in Se-CCF film. These results indicate that the bulk crystallization of the CZTSSe film can be improved by reducing the Se temperature.

Based on the normalized Raman spectra (Fig. 1(c)), the defect properties of the CZTSSe films can be analyzed. As reported in literature, the presence of V_{Cu} and Zn_{Cu} defects in CZTSSe can enhance the B vibrational modes (at around 170 cm^{-1}), while the presence of Sn_{Zn} defect can cause the conversion of B vibrational modes (at around 250 cm^{-1}) to E vibrational modes (at around 220 cm^{-1}) [38]. According to the Raman spectra, the reduced Se temperature decreases the Raman intensity at 220 cm^{-1} but increases the Raman intensity at 250 cm^{-1}. Besides, the peak fitting results of Raman spectra (Fig. S3 in the ESM) prove the relative intensity of the 170 cm^{-1} peak decreases with the decrease of Se temperature. Therefore, the decreased Se temperature could reduce the concentration of the shallow acceptor V_{Cu} and the deep-level defect Sn_{Zn} in CZTSSe film. Due to the decreased concentration of Sn_{Zn} defect, the carrier recombination in Se-CCF film could be alleviated, which is beneficial to the performance of CZTSSe solar cell.

Figures 2(a)–2(d) show the statistic parameters of the CZTSSe solar cells (the parameters of the best solar cells are listed in Table 1). It is found that the open-circuit voltages (V_{OC}), short-circuit current densities (J_{SC}), fill factors, and efficiencies of the solar

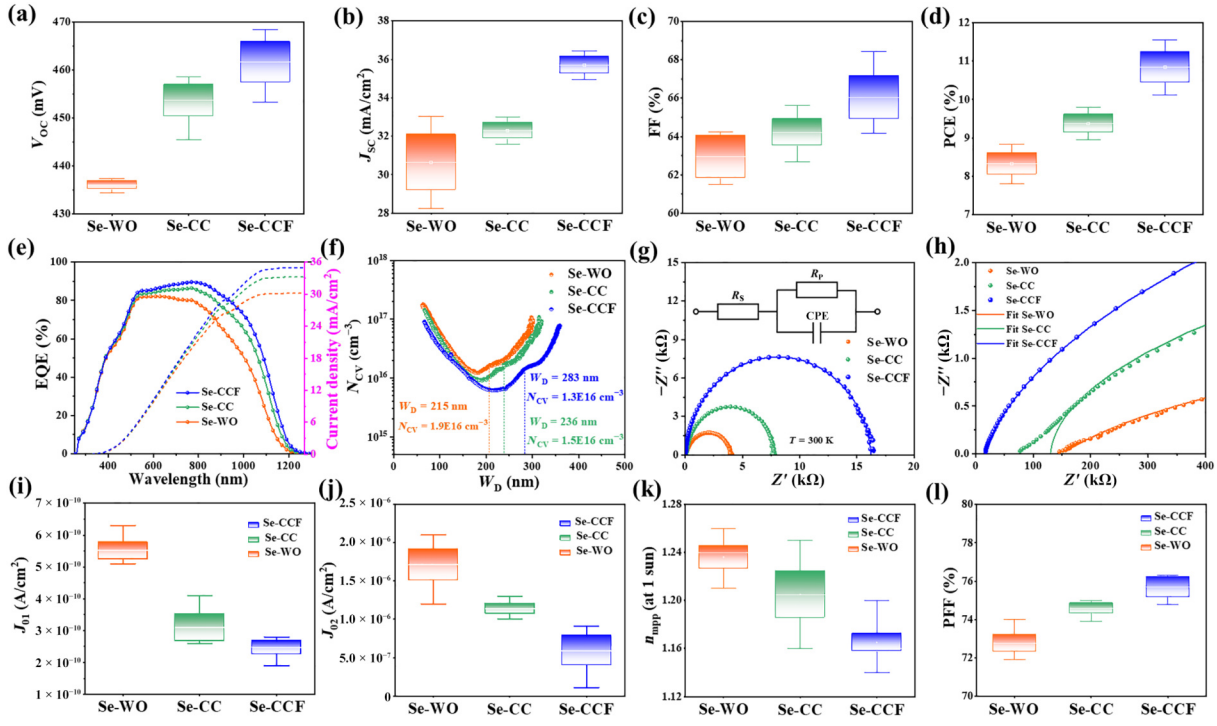

Figure 2 (a)–(d) Statistics of the solar cell parameters. (e) EQE curves of the best solar cells. (f) Doping profiles of the CZTSSe absorber layers. (g) and (h) Impedance spectra of the solar cells. (i)–(l) Suns-V_{OC} analyses of the solar cells.

Table 1 The device parameters of the best solar cells

	V_{OC} (mV)	J_{SC} (mA/cm^2)	FF (%)	PCE(%)	W_D (nm)	R_S (Ω)
Se-WO	436.4	32.0	62.5	8.7	215	150
Se-CC	456.6	32.9	64.7	9.7	236	80
Se-CCF	468.3	36.3	66.6	11.3	283	16

cells are all improved by decreasing Se temperature. The EQE results (Fig. 2(e)) show that the reduced Se temperature mainly enhances EQE in the wavelength region above 500 nm. This might be caused by the enlarged depletion width (W_D) of the solar cell (Fig. 2(f), W_D increases from 215 nm for Se-WO solar cell to 283 nm for Se-CCF solar cell), as well as the improved crystallinity of the CZTSSe layer (the enhanced crystallization in bulk can reduce the defective grain-boundaries, thus suppressing the carrier recombination and increasing the diffusion length of the photo-carriers). Consequently, more photo-carriers can be collected by the solar cell, which results in the increased J_{SC} (J_{SC} increases from 32.0 mA/cm^2 for Se-WO solar cell to 36.3 mA/cm^2 for Se-CCF solar cell).

To estimate the carrier recombination of the solar cells, the solar cells are characterized by EIS (Figs. 2(g) and 2(h)) and Suns-V_{OC} tests (Figs. 2(i)–2(l)). In the EIS curve, the intercept of the curve on real axis represents the series resistance (R_S), while the diameter of the curve equals to recombination resistance (R_P) of the solar cell [39]. By comparing the EIS data, it is found the reduced Se temperature can decrease R_S but increase R_P of the solar cell. The variation of R_S and R_P may relate to the different crystallinity of the CZTSSe layer. As shown in SEM images of the films (Fig. 1(e)), the bulk crystallinity of CZTSSe film is improved by reducing Se temperature. Therefore, the defective grain-boundaries which can inhibit carrier transport and enhance carrier recombination could be reduced in Se-CCF film. As a result, the carrier transport could be enhanced but the carrier recombination could be suppressed in Se-CCF solar cell, which result in decreased R_S but increased R_P (additionally, the reduced Sn_{Zn} defects in Se-CCF film are another reason for the increased R_P of the Se-CCF solar cell).

The Suns-V_{OC} test shows that both J_{01} and J_{02} of the solar cell are reduced by decreasing Se temperature. The J_{01} and J_{02} derived from the Suns-V_{OC} test can represent the carrier recombination in neutral region and depletion region of the solar cell, respectively [40]. Accordingly, both the carrier recombination in neutral region and depletion region of the CZTSSe solar cell are reduced with decreased Se temperature (could be caused by the improved crystallinity and suppressed deep-level defects of the CZTSSe absorber). Besides, the reduced Se temperature can decrease the ideality factor of the solar cell (Fig. 2(k)), which could be caused by the suppressed carrier recombination in depletion region of the solar cell. Both the EIS and Suns-V_{OC} tests prove that the decreased Se temperature can suppress the carrier recombination in CZTSSe solar cell. As a result, the V_{OC} of the solar cell can be increased (from 436.4 mV for Se-WO solar cell to 468.3 mV for Se-CCF solar cell). The increased V_{OC}, the decreased ideality factor, and the reduced R_S could increase the fill factor of the solar cell (62.5% for Se-WO solar cell to 66.6% for Se-CCF solar cells). Eventually, the efficiency of the solar cell (power conversion efficiency (PCE)) increases from 8.7% (Se-WO) to 11.3% (Se-CCF).

3.2 Effect of Se temperature on the crystallization of CZTSSe film

Figures 3(a)–3(c) show the XRD patterns and Raman spectra of the half-selenized films (the temperature profiles of the half-selenized films can be seen in Fig. S2 in the ESM). It is found that the (112) diffraction peaks of the half-selenized films shift from 28.5° to 27.2° as the increase of selenization temperature, which can be attributed to the substitution of S by Se (as Se has a larger ionic radius than S,

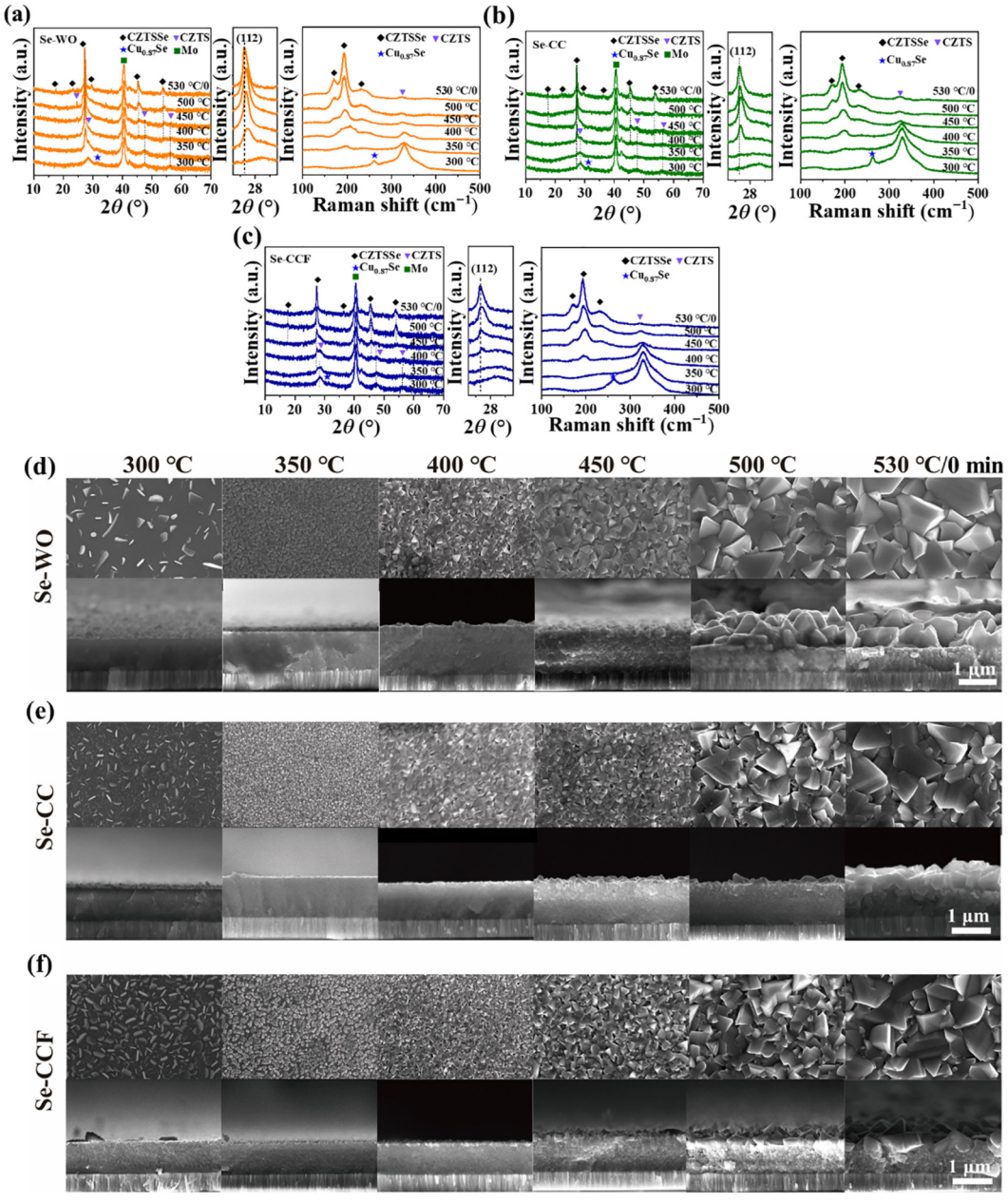

Figure 3 (a)–(c) XRD patterns and Raman spectra of the half-selenized films. (d)–(f) SEM images of the half-selenized films.

S-to-Se substitution can cause the expansion of lattice). Besides, the results reveal that the reduced Se temperature can delay the formation of CZTSSe in selenization process. For Se-Wo and Se-CC films, the intrinsic XRD and Raman peaks of CZTSSe emerge at 350 and 400 °C, respectively. However, only weak intrinsic XRD peaks of CZTSSe are detected in Se-CCF film at 400 °C (the peak fitting results of the half-selenized films at 400 °C can be seen in Fig. S4 in the ESM). These indicate the different transitions from CZTS to CZTSSe, which could be attributed to the different Se partial pressure (caused by different Se temperatures) and may affect the crystallization of CZTSSe films [41].

Figures 3(d)–3(f) show the SEM images of the half-selenized films (the variation of the film thicknesses in SEM images may result from the inhomogeneous thickness of the spin-coated precursor film, the volume expansion of the film due to S-to-Se substitution, as well as the roughness caused by the growth of surficial crystalline grains). The results reveal that reduced Se temperature can increase the quantity but decrease the sizes of crystalline grains at temperature below 500 °C (i.e., early-stage crystallization), which may be related to different transitions from CZTS to CZTSSe (i.e., different generations of Cu_xSe) and different generations of liquid Se. According to the crystallization model proposed by Hages, Se vapor can condense in precursor film during the selenization process. Then the condensed liquid Se can induce the formation of Cu_xSe, which may facilitate the nucleation of CZTSSe grains [42]. Herein, the SEM, XRD, and Raman results prove that Cu_xSe crystalline grains can be generated on the films at 350 °C. By decreasing the Se temperature, the Cu_xSe grains can distribute more homogeneously on the film, which may enhance the nucleation of the CZTSSe grains. Besides, XPS characterizations reveal that elemental Se can condense on the surfaces of the films at 400–450 °C, and the amount of the condensed liquid Se can be

reduced by decreasing Se temperature (Fig. S5 in the ESM). Considering that liquid Se may assist elemental diffusion during the early-stage crystallization of the CZTSSe film, less liquid Se would suppress the elemental diffusion of the film. With enhanced nucleation and suppressed elemental diffusion, the number of CZTSSe grains can be increased but the sizes of the CZTSSe grains are reduced.

SEM images reveal that the crystallization of CZTSSe film mainly occurs at temperatures above 500 °C (i.e., late-stage crystallization), which is affected by the Se temperature. Figures 1(e) and 3(d)–3(f) reveal that the decreased Se temperature can enhance the bulk crystallization of CZTSSe film at temperature above 500 °C, which might be caused by the liquid-intermedia-phase assisted crystallization. Figure 4(a) shows the S/(S+Se) ratios of the half-selenized films as the variation of selenization temperature. The data prove that the decreased Se temperature can delay the S-to-Se substitution of the film to higher temperature. Figure 4(b) shows the depth S/Se XPS profiles of the half-selenized films at 500 °C. The results prove that more S can remain at bottom of the film by decreasing Se temperature. Thus, more S-to-Se substitution would occur at the bottom of Se-CCF film than that of the other films at elevated temperature. According to previous work, liquid-intermedia-phase could be generated by S-to-Se substitution at temperatures above 500 °C [33, 34]. Therefore, obvious liquid-intermedia-phase could be generated in Se-CCF film, which eliminates the fine-grain layer of the film by enhancing the bulk

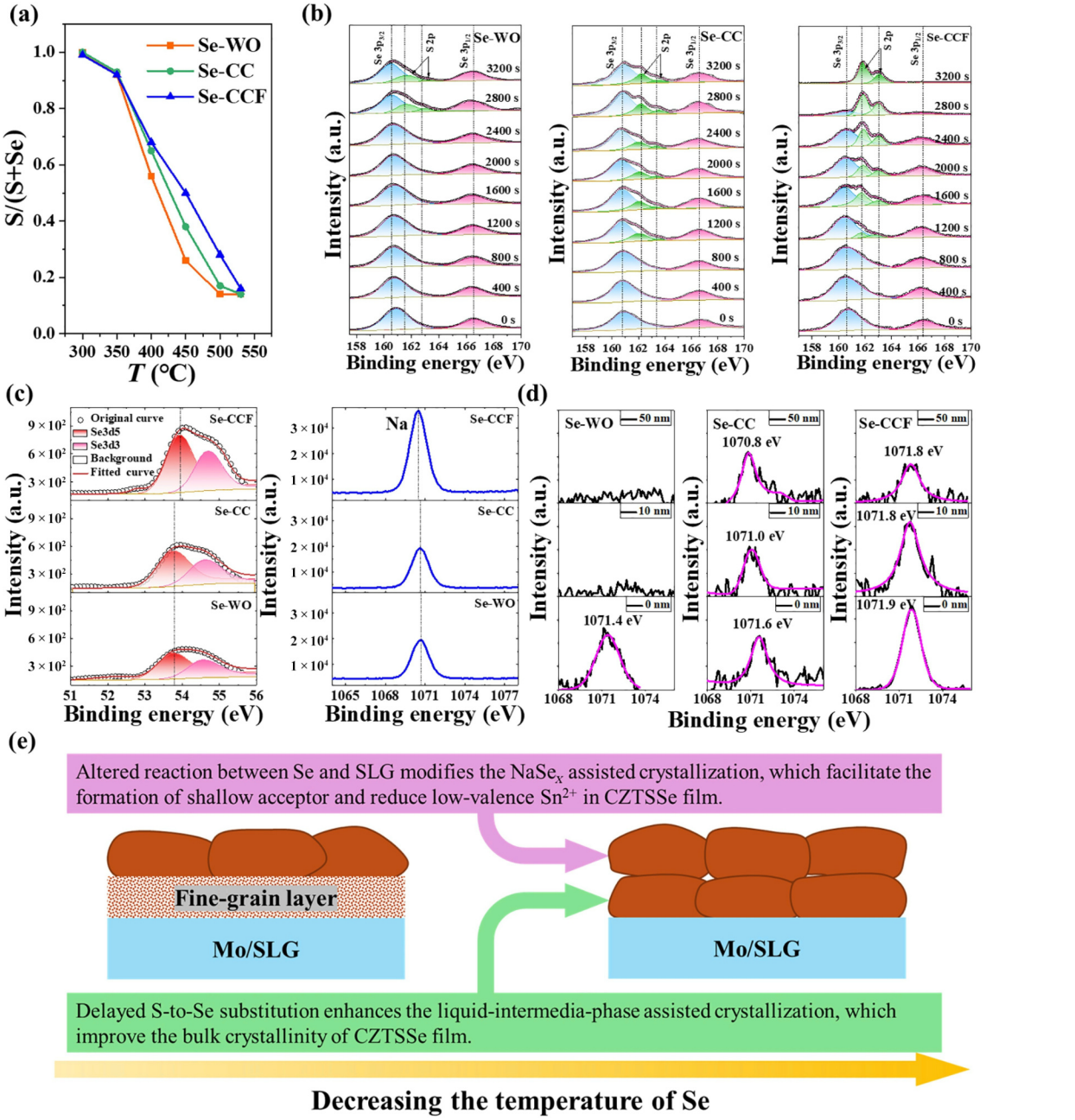

Figure 4 (a) Variation of S/(S+Se) ratios in half-selenized films as selenization temperature. (b) Depth S and Se XPS profiles in half-selenized films that selenized at 500 °C. (c) XPS characterization on quartz glass after simulated selenization. (d) Depth Na XPS profiles in the CZTSSe films. (e) Mechanism that how the Se temperature affect the crystallization of CZTSSe film.

crystallization. As a comparison, fine-grain layer remains in Se-WO and Se-CC films, which could be caused by the insufficient generation of liquid-intermedia-phase.

The Raman data (Figs. 1(c) and 1(d), and Table S1 in the ESM) reveal that the surficial crystallinity can be improved by decreasing Se temperature. This result indicates that Se temperature may affect the $NaSe_x$ assisted crystallization of CZTSSe film because such mechanism dominates the surficial crystallization of CZTSSe film at high temperatures (e.g., > 500 °C). As reported in literature, gaseous $NaSe_x$ can form via the reaction between Se vapor and Na-contained matter (e.g., SLG substrate) in selenization process [43]. Then the gaseous $NaSe_x$ could condense and transfer to liquid $NaSe_x$ flux on CZTSSe film. In previous work, it was proposed to regulate the reaction between Se and sodium source by changing the type of sodium source that was added in the selenization process. As a result, the formation of gaseous $NaSe_x$ and the properties of $NaSe_x$ flux were altered, which modified the $NaSe_x$ assisted crystallization of CZTSSe film [35]. Alternatively, the reaction between Se and SLG substrate may be regulated by adjusting the Se temperature. Thus, the formation of gaseous $NaSe_x$ and the transition from gaseous $NaSe_x$ to liquid $NaSe_x$ could be modified, which may yield $NaSe_x$ fluxes with different properties (according to the p-T phase diagram of selenide compound such as Cu-Se system, the partial pressure of Se is an important factor that determines the type and properties of the selenide compound. Similarly, the different Se partial pressures of the selenizations may alter the formation and properties of $NaSe_x$) [44]. Figure 4(c) shows the XPS characterizations on quartz glass after simulated selenization processes (i.e., quartz glass is used instead of precursor film for selenization). For all the samples, Na and Se XPS peaks can be detected. However, the positions of the Na and Se XPS peaks, as well as their relative intensities are different. These results indicate that $NaSe_x$ can be generated on quartz glass slides, but their properties are different depending on the Se temperature. Similarly, $NaSe_x$ flux with different properties could be generated on CZTSSe films by modifying the Se temperature, which facilitates the regulation over $NaSe_x$ assisted crystallization of CZTSSe film.

One of the proofs for the varied $NaSe_x$ assisted crystallization of CZTSSe film is the different Na-incorporations in CZTSSe films. Figure 4(d) shows the Na XPS depth profiles for the CZTSSe films (to compare the data, the start scale and end scale of all the *y* axes are identical). It is found that sodium only exists on the surface of Se-WO film. However, sodium can incorporate into Se-CC and Se-CCF films. Besides, the intensities of Na XPS peaks are different between Se-CC and Se-CCF films, indicating that the Na-incorporations are different between the films. These results suggest that the kinetic processes of $NaSe_x$ assisted crystallizations may be changed (caused by different properties of $NaSe_x$ fluxes).

3.3 Analysis on defect and interfacial properties of CZTSSe solar cell prepared with different Se temperatures

Figure 5(a) shows the admittance spectra, the estimated acceptor levels and the defect spectra of the CZTSSe solar cells. The Se-WO film mainly contains defect with the energy level of 188 meV (could be attributed to the Zn_{Sn} defect) [45, 46]. In contrast, the Se-CC film contains defects with the energy levels of 186 meV (Zn_{Sn} defect) and 75 meV (could be attributed to the V_{Zn} defect), while the Se-CCF film contains defects with the energy levels of 81 meV (V_{Zn} defect) and 21 meV (could be attributed to the V_{Cu} or the Na_{Zn} defect) [45, 46]. Accordingly, the reduced Se temperature can facilitate the formation of shallow level acceptors, which might be caused by the varied $NaSe_x$ assisted crystallization of CZTSSe film. It has been reported that deep acceptors in depletion region may enhance the carrier recombination of the solar cell [47]. Thus, the shallow level acceptor in Se-CCF could alleviate the carrier recombination of the solar cell.

Figure 5(b) shows the Urbach tail energy (E_u) of the CZTSSe films (estimated from EQE data). The E_U of CZTSSe film slightly decreases as the decrease of Se temperature, which may result from the improved bulk crystallinity of the film (caused by enhanced liquid-intermedia-phase assisted crystallization). Ultimately, the emergence of shallow level acceptors and the decreased E_U prove that the defect properties of CZTSSe film can be improved by

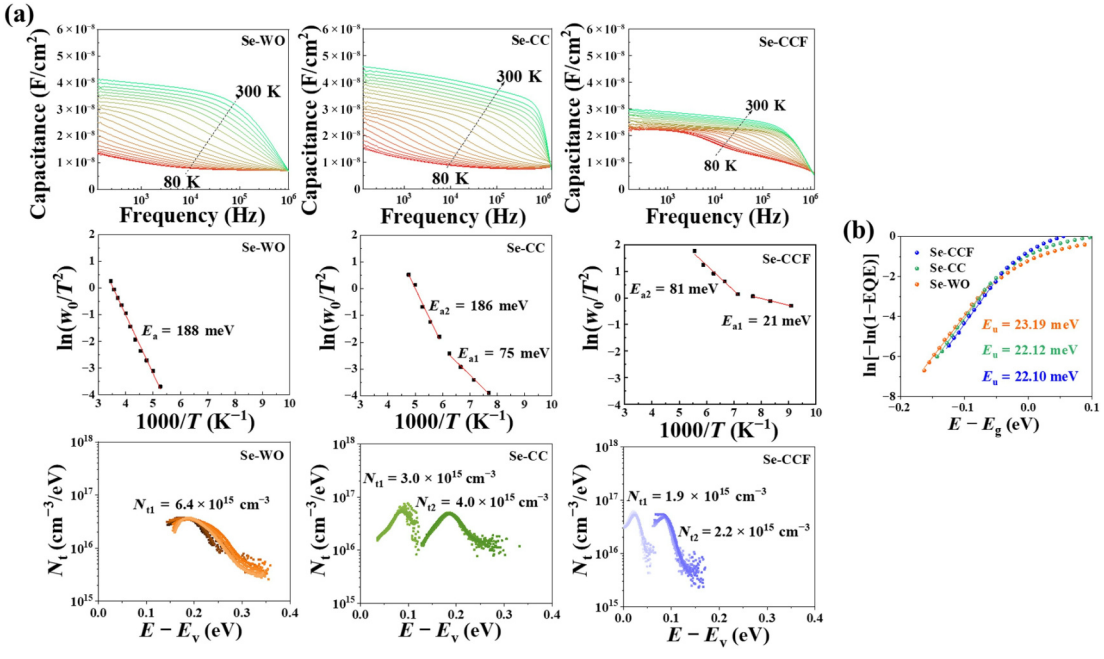

Figure 5 (a) Admittance spectra and related analyses of CZTSSe solar cells. (b) Estimation of the band tail energies for CZTSSe films.

decreasing Se temperature. These are beneficial to the performances of CZTSSe solar cells [48, 49].

The Se temperature can also influence the interfacial properties of CZTSSe solar cell due to the modified surficial and bulk crystallization of CZTSSe film. Figure 6 shows the temperature dependent *I*–*V* curves of the CZTSSe solar cells. Based on the data, the activation energy for the main recombination path (E_R), as well as the back contact barrier (Φ_B) of the solar cell are estimated [50]. It is found the decreased Se temperature can increase E_R (from 0.97 eV for Se-WO to 1.04 eV for Se-CCF) but decrease Φ_B of the solar cell (from 94 meV for Se-WO to 48 meV for Se-CCF). The increased E_R may be caused by the modified crystallization and Na-incorporation of the surficial layer, while the decreased Φ_B could be related to the improved crystallinity of the bottom layer. Generally, the increased E_R indicates that the conduction band offset at the absorber/buffer interface is improved. This can reduce the carrier recombination around the absorber/buffer interface. The decreased Φ_B implies that the carrier transport at the back contact (CZTSSe/Mo) is enhanced. Both the increased E_R and decreased Φ_B help to improve the performance of CZTSSe solar cell.

The results above clearly prove that the crystallization and properties of CZTSSe film can be optimized by decreasing the temperature of Se source. It should be noted that the Se temperature is not optimized to the best condition in this work, i.e., the bi-layer structure which contains a defective boundary between the top and bottom layers still exists in the Se-CCF films. This indicates that the generation of the liquid-intermedia-phase is not sufficient in the selenization process. A fine adjustment of the Se temperature with large adjustable region may help to solve the problem. We will explore the approaches which can well control the Se temperature in the future (e.g., finely controlling the thickness or thermal conductivity of the ceramic parts).

3.4 Effect of Se temperature on enhanced $NaSe_x$ assisted crystallization and properties of CZTSSe film

Alternatively, we tried to optimize the crystallization of CZTSSe film by enhancing the $NaSe_x$ assisted crystallization. Based on previous investigation, an additional Na_2S source for selenization can yield $NaSe_x$ with suitable properties by modifying the reaction between sodium-contained matters and Se [35]. Figure S6 in the ESM shows the XPS characterizations on quartz glass after simulated selenization processes (with and without Na_2S source). The results indicate that the addition of Na_2S source can obviously change the properties of $NaSe_x$ flux (i.e., the positions and shapes of Na and Se XPS peaks are significantly altered by the Na_2S source). Consequently, the $NaSe_x$ assisted crystallization of CZTSSe film could be modified by the altered properties of $NaSe_x$ flux. The CZTSSe films selenized with additional Na_2S are named as Se-WO-Na (Se on graphite), Se-CC-Na (Se on ceramic crucible) and Se-CCF-Na (Se on ceramic crucible and ceramic slice).

Figures 7(a) and 7(b) show XRD patterns and Raman spectra of CZTSSe films (selenized with Na_2S, after whole selenization process). The FWHM of the (112) XRD peaks and the 197 cm^{-1} Raman peaks for the CZTSSe films are listed in Table S1 in the ESM and plotted in Fig. 7(c). Generally, the addition of Na_2S can reduce FWHM of XRD and Raman peaks, indicating that the crystallinities of the CZTSSe films are enhanced. Nevertheless, the FWHM of XRD peak for Se-CCF-Na is increased compared to that

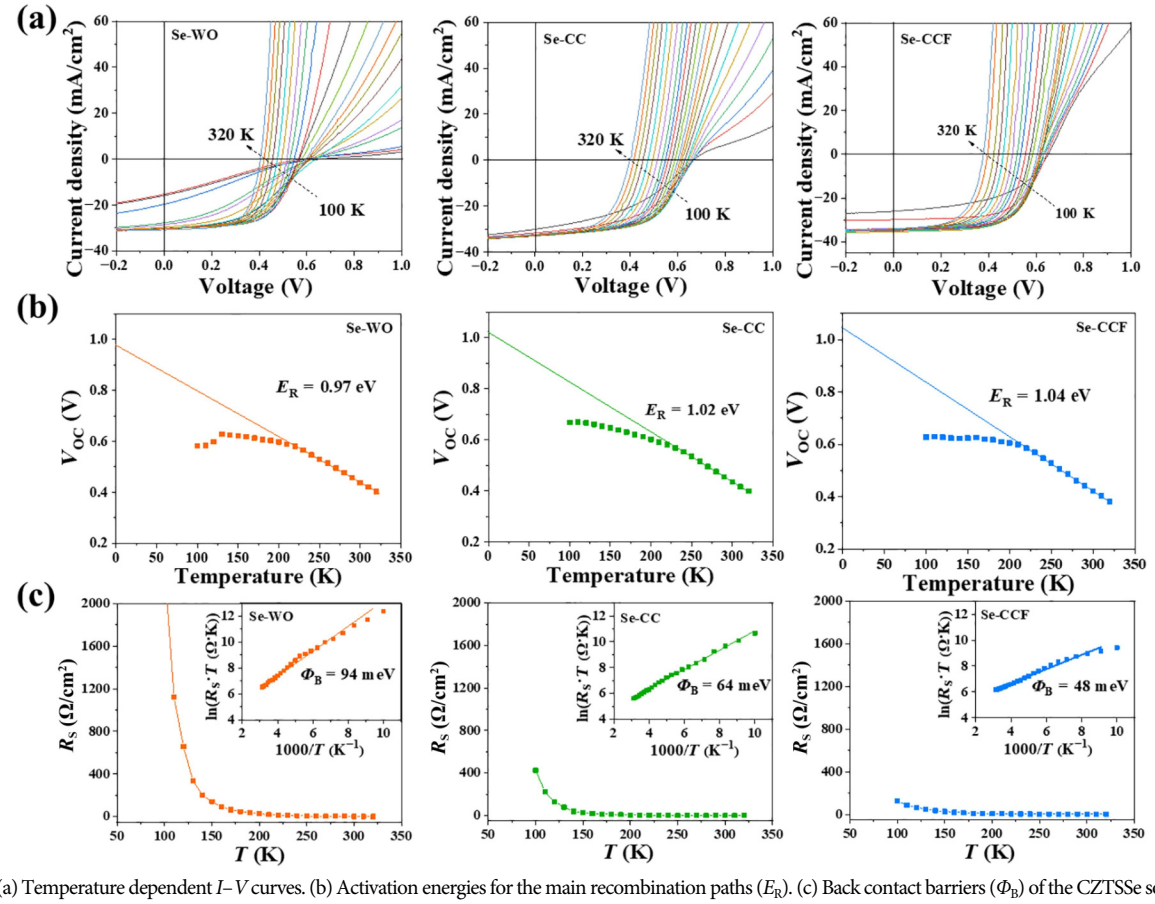

Figure 6 (a) Temperature dependent *I*–*V* curves. (b) Activation energies for the main recombination paths (E_R). (c) Back contact barriers (Φ_B) of the CZTSSe solar cells.

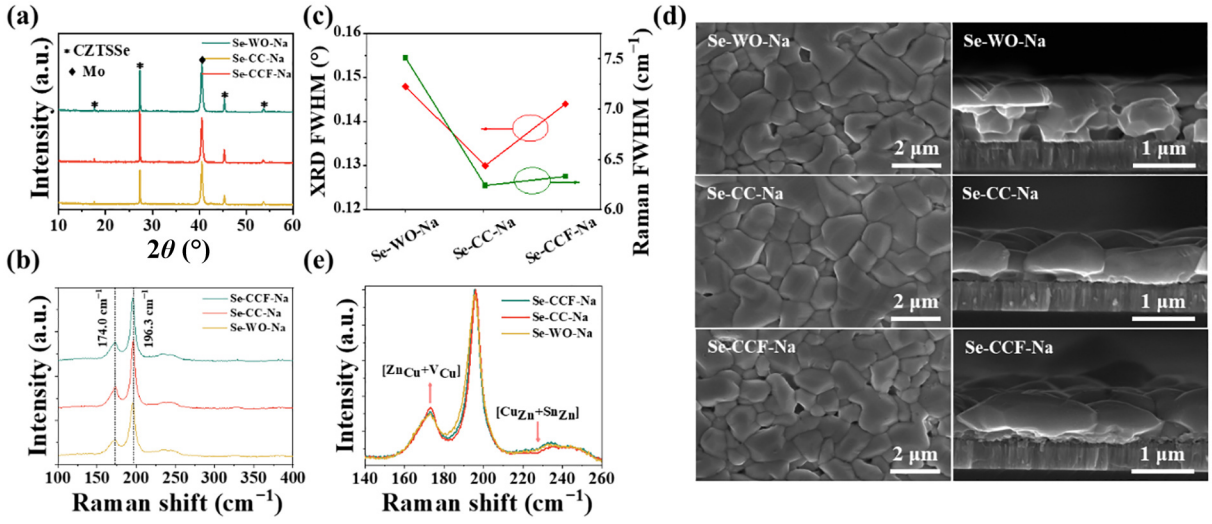

Figure 7 (a), (b), and (e) XRD patterns and Raman spectra of the CZTSSe films (with additional Na_2S source). (c) FWHM of the (112) diffraction peaks and Raman peaks at 197 cm^{-1}. (d) SEM images of the CZTSSe films.

for Se-CCF, indicating that the introduction of Na_2S could deteriorate the crystallinity for Se-CCF film. SEM images of the CZTSSe films (Fig. 7(d)) show that the morphology of CZTSSe films are improved by adding Na_2S source. The altered crystallinity and morphology of CZTSSe film by Na_2S suggest that the crystallization of CZTSSe film is changed, which may cause the variation of the lattice defects in CZTSSe film. Figure S7 in the ESM shows the admittance spectra of Se-CC and Se-CC-Na solar cells. Based on the data, the acceptor levels of the CZTSSe films are estimated (156 and 75 meV for Se-CC film, while 99 and 26 meV for Se-CC-Na). Therefore, the addition of Na_2S for selenization can facilitate the formation of shallow level acceptor.

By comparing the admittance data, it is found that decreasing the Se temperature (Se-CC vs. Se-CCF) and using additional Na_2S source (Se-CC vs. Se-CC-Na) have similar effects on the formation of electrically active defects. In previous investigation, it is found the $NaSe_x$ assisted crystallization may be dominated by the properties of $NaSe_x$ flux, which can be affected by the reaction between sodium source and Se. According to Le Chatelier's principle, decreasing the temperature of Se source (decreases the Se supply) and using additional Na_2S source (increases the Na supply) could play similar role in shifting the chemical equilibrium of the reaction between sodium source and Se. Therefore, decreasing Se temperature or adding Na_2S source may cause $NaSe_x$ flux with similar properties. It is believed the similar formations of lattice defects could be caused by the similar properties of $NaSe_x$ fluxes.

For CZTSSe films selenized with Na_2S, the Se temperature can still be an influence factor for the crystallization of the film. In this condition, the bulk crystallization of CZTSSe film may be affected by both the S-to-Se substitution and the properties of $NaSe_x$ flux. For Se-CC-Na film, the uniform morphology of the film could be caused by the optimum properties of $NaSe_x$ flux, as well as the coordination between S-to-Se substitution and generation of $NaSe_x$ flux. Unlike the Se-CC-Na film (in which the mono-layer morphology is achieved), the bi-layer structures still exist in Se-WO-Na and Se-CCF-Na films, which might be caused by the unfavorable properties of $NaSe_x$, and/or the discoordination between S-to-Se substitution and generation of $NaSe_x$ flux. Besides, the FWHM of XRD and Raman peaks are different among the CZTSSe films (Fig. 7(c), indicating that Se temperature affects both S-to-Se substitution and formation of $NaSe_x$ flux, thereby influencing the crystallization of CZTSSe film. Except that, the normalized Raman spectra (Fig. 7(e)) reveal that the defect properties are different among the CZTSSe films (i.e., Se-CC-Na film would contain more V_{Cu} defects and less Sn_{Zn} defects compared to Se-WO-Na and Se-CCF-Na films). Accordingly, by synergistically modifying the Se source (Se temperature) and the Na source (additional Na_2S), the crystallinity, morphology, and defect properties of CZTSSe film (Se-CCF-Na) are improved simultaneously. This may yield solar cells with higher efficiencies.

It should be noted that the optimum Se temperatures for CZTSSe films selenized with and without Na_2S are different. As discussed above, Se temperature can simultaneously affect liquid-intermedia-phase assisted crystallization and $NaSe_x$ assisted crystallization of CZTSSe film. Due to different work principles, the optimum Se temperatures for these two crystallization mechanisms might be different. The optimum Se temperature for selenization should be between the optimum Se temperatures for liquid-intermedia-phase assisted crystallization and $NaSe_x$ assisted crystallization. When Na_2S source is added for selenization, the chemical equilibrium of the reaction between sodium-contained matters and Se are shifted, which may alter the properties of $NaSe_x$ (Fig. S6 in the ESM). Therefore, the optimum Se temperature for $NaSe_x$ assisted crystallization could be changed by the addition of Na_2S. Besides, the addition of Na_2S for selenization can enhance the $NaSe_x$ assisted crystallization of CZTSSe film. Thus, the optimum Se temperature for selenization may shift to the optimum Se temperature for $NaSe_x$ assisted crystallization. The different optimum temperatures for CZTSSe films prepared with and without Na_2S could be attributed to the above reasons.

Figure 8 shows the *I*–*V* curves, QE curves, EIS, and Suns-V_{OC} test results of the CZTSSe solar cells (prepared with Na_2S), the parameters of the best solar cells are listed in Table 2 (the statistics of the solar cell parameters are shown in Fig. S8 in the ESM). Compared to solar cells prepared without Na_2S, the solar cells prepared with Na_2S exhibit smaller series resistance (R_S) and improved EQE in long wavelength region (especially for Se-WO-Na and Se-CC-Na solar cells). This could be caused by the improved bulk crystallization of the CZTSSe films. Besides, the Se temperature can obviously affect the performances of CZTSSe solar

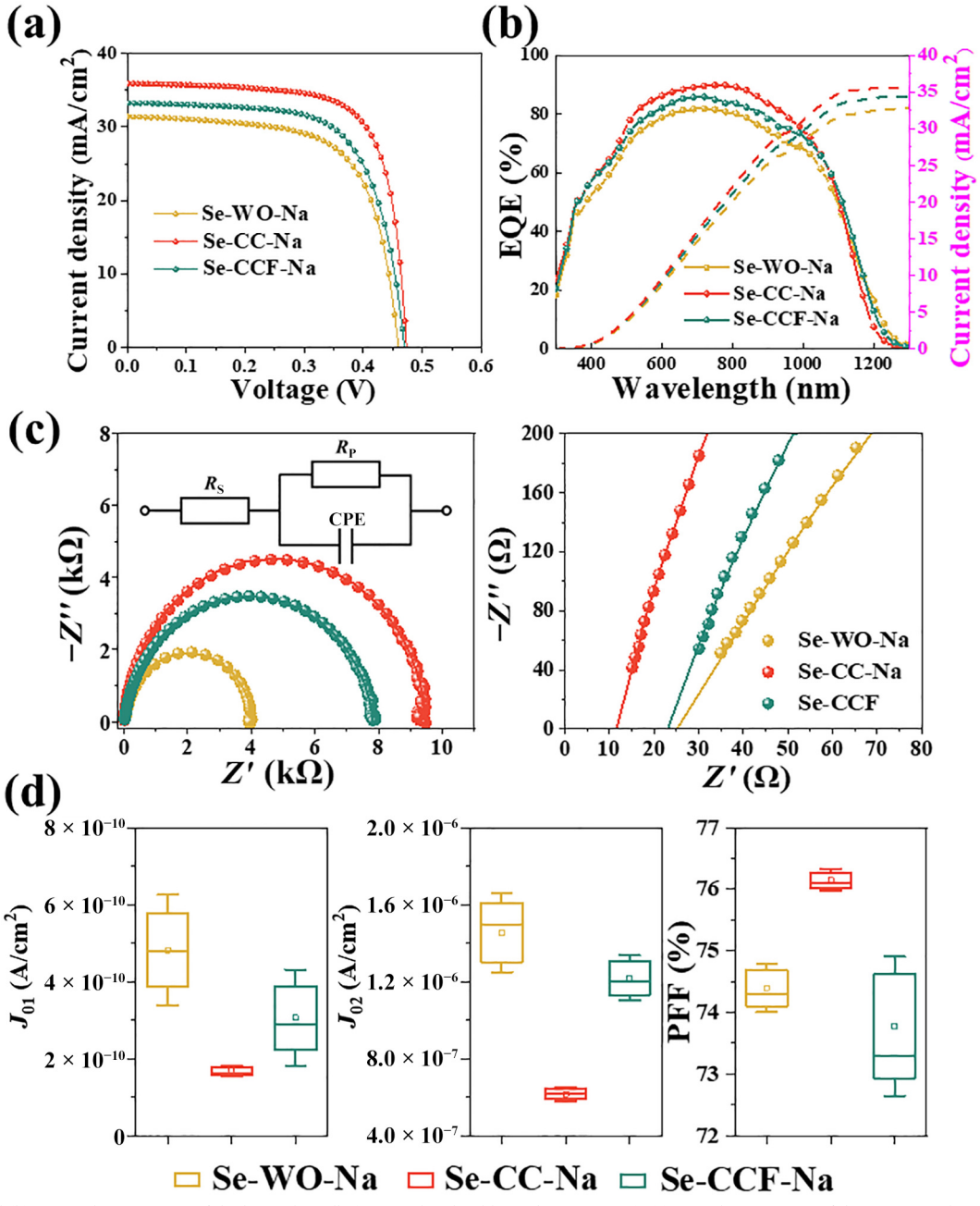

Figure 8 (a) and (b) *I*–*V* and EQE curves of the best solar cells (prepared with additional Na_2S source). (c) Impedance spectra of the CZTSSe solar cells. (d) Suns-V_{OC} analyses of the CZTSSe solar cells.

cells. Compared to Se-WO-Na and Se-CCF-Na solar cells, the Se-CC-Na solar cell exhibits obviously decreased recombination resistance (R_P) and reverse saturation current densities (J_{01} and J_{02}). These results indicate that the carrier recombination in Se-CC-Na solar cells are suppressed, which can be attributed to the improved crystallinity, morphology, and defect properties of the Se-CC-Na films. Consequently, the performance of the Se-CC-Na solar cell is improved, which achieves the best efficiency of 12.3%.

Table 2 Device parameters for the best CZTSSe solar cells (prepared with Na_2S source)

	V_{OC} (mV)	J_{SC} (mA/cm²)	FF (%)	PCE (%)	R_S (Ω)
Se-WO-Na	459.9	31.4	65.3	9.4	25
Se-CC-Na	473.2	35.9	72.2	12.3	12
Se-CCF-Na	469.7	33.3	67.3	10.5	23

4 Conclusion

This paper reveals the effect of Se source temperature on the different crystallization mechanisms of CZTSSe film. On one hand, the Se temperature can affect the S-to-Se substitution of the film in the selenization process. By decreasing Se temperature, the S-to-Se substitution can be delayed to higher temperature. This may facilitate the formation of liquid-intermedia-phase, which can improve the bulk crystallization of the film. On the other hand, the Se temperature can influence the reaction between Se and the Na source (SLG or Na_2S). This can modify the properties of the $NaSe_x$

flux that generated on the film, thus affecting the $NaSe_x$ assisted crystallization of the film. By synergistically modifying the Se source (Se temperature) and the Na source (additional Na_2S) for selenization, the coordination between liquid-intermedia-phase assisted crystallization and $NaSe_x$ assisted crystallization of CZTSSe film could be achieved. Consequently, the crystallinity, morphology and defect properties of the CZTSSe film are improved simultaneously. This yields solar cells with the best efficiency of 12.3%.

Electronic Supplementary Material: Supplementary material (thermal imaging tests of Se pellets and crucible parts, XPS characterizations for half-selenized films and simulated selenization, admittance data for Se-CC and Se-CC-Na solar cells and statistics of solar cell parameters) is available in the online version of this article at https://doi.org/10.26599/NR.2025.94907791.

Data availability

All data needed to support the conclusions in the paper are presented in the manuscript and the Electronic Supplementary Material. Additional data related to this paper may be requested from the corresponding author upon request.

Acknowledgements

This work is granted by the National Key R&D Program of China (No. 2022YFE0196100), Local Science and Technology Development Fund Projects Guided by the Central Government (No. 236Z4305G), the Natural Science Foundation of Hebei Province (No. F2023201025), the Hebei Province Optoelectronic Information Materials Laboratory Performance Subsidy Fund Project (No. 22567634H), and the Open bidding for selecting the best candidates of Baoding (No. 2023chuang206).

Declaration of competing interest

All the contributing authors report no conflict of interests in this work.

Author contribution statement

C. G.: Conceptualization, supervision, funding acquisition. Y. J. M.: Investigation, writing – original draft. Y. L.: Investigation, validation. Y. X. H.: Resources. C. S.: Resources. R. Z.: Resources. Q. Z.: Resources. X. Z. W.: Funding acquisition. W. Y.: Project administration, funding acquisition. Z. Q. L.: Supervision, writing – review & editing. All the authors have approved the final manuscript.

Use of AI statement

None.

References

[1] Fu, J. J.; Yang, J.; Dong, W. W.; Ren, S.; Zhu, H. N.; Wang, Y. S.; Hao, J. C.; Wu, J. H.; Wang, R. Z.; Zhao, D. D. et al. A critical review of solution-process engineering for Kesterite thin-film solar cells: Current strategies and prospects. *J. Mater. Chem. A* **2024**, *12*, 545–566.

[2] Xie, W. H.; Yan, Q.; Sun, Q. Z.; Li, Y. F.; Zhang, C. X.; Deng, H.; Cheng, S. Y. A progress review on challenges and strategies of flexible $Cu_2ZnSn(S,Se)_4$ solar cells. *Sol. RRL* **2023**, *7*, 2201036.

[3] Zhao, Y. H.; Chen, S.; Su, Z. H.; Luo, J. T.; Zhang, X. H.; Liang, G. X. Research progress of Kesterite solar cells. *Chin. Sci. Bull.* **2023**, *68*, 4662–4673.

[4] Sun, K. W.; Huang, J. L.; Li, J. J.; Yan, C.; Hao, X. J. Recent progress in defect engineering for Kesterite solar cells. *Sci. China Phys. Mech. Astron.* **2023**, *66*, 217302.

[5] Giraldo, S.; Jehl, Z.; Placidi, M.; Izquierdo-Roca, V.; Pérez-Rodríguez, A.; Saucedo, E. Progress and perspectives of thin film Kesterite photovoltaic technology: A critical review. *Adv. Mater.* **2019**, *31*, 1806692.

[6] He, M. R.; Yan, C.; Li, J. J.; Suryawanshi, M. P.; Kim, J.; Green, M. A.; Hao, X. J. Kesterite solar cells: Insights into current strategies and challenges. *Adv. Sci.* **2021**, *8*, 2004313.

[7] Pal, K.; Singh, P.; Bhaduri, A.; Thapa, K. B. Current challenges and future prospects for a highly efficient (> 20%) Kesterite CZTS solar cell: A review. *Sol. Energy Mater. Sol. Cells* **2019**, *196*, 138–156.

[8] Green, M. A.; Dunlop, E. D.; Yoshita, M.; Kopidakis, N.; Bothe, K.; Siefer, G.; Hinken, D.; Rauer, M.; Hohl-Ebinger, J.; Hao, X. J. Solar cell efficiency tables (Version 64). *Prog. Photovoltaics* **2024**, *32*, 425–441.

[9] Duan, B. W.; Shi, J. J.; Li, D. M.; Luo, Y. H.; Wu, H. J.; Meng, Q. B. Underlying mechanism of the efficiency loss in CZTSSe solar cells: Disorder and deep defects. *Sci. China Mater.* **2020**, *63*, 2371–2396.

[10] Gong, Y. C.; Xin, H.; Ding, L. M. V_{oc} deficit in Kesterite solar cells. *J. Semicond.* **2021**, *42*, 100201.

[11] Grenet, L.; Suzon, A. A.; Emieux, F.; Roux, F. Analysis of failure modes in Kesterite solar cells. *ACS Appl. Energy Mater.* **2018**, *1*, 2103–2113.

[12] Li, J. J.; Huang, J. L.; Ma, F. J.; Sun, H.; Cong, J. L.; Privat, K.; Webster, R. F.; Cheong, S.; Yao, Y.; Chin, R. L. et al. Unveiling microscopic carrier loss mechanisms in 12% efficient $Cu_2ZnSnSe_4$ solar cells. *Nat. Energy* **2022**, *7*, 754–764.

[13] Chen, S. Y.; Walsh, A.; Gong, X. G.; Wei, S. H. Classification of lattice defects in the Kesterite Cu_2ZnSnS_4 and $Cu_2ZnSnSe_4$ earth-abundant solar cell absorbers. *Adv. Mater.* **2013**, *25*, 1522–1539.

[14] Shin, D.; Saparov, B.; Mitzi, D. B. Defect engineering in multinary earth-abundant chalcogenide photovoltaic materials. *Adv. Energy Mater.* **2017**, *7*, 1602366.

[15] Wei, H.; Li, Y. M.; Cui, C. C.; Wang, X.; Shao, Z. P.; Pang, S. P.; Cui, G. L. Defect suppression for high-efficiency Kesterite CZTSSe solar cells: Advances and prospects. *Chem. Eng. J.* **2023**, *462*, 142121.

[16] Tian, Q. W.; Liu, S. Z. Defect suppression in multinary chalcogenide photovoltaic materials derived from Kesterite: Progress and outlook. *J. Mater. Chem. A* **2020**, *8*, 24920–24942.

[17] Shi, J. J.; Wang, J. L.; Meng, F. Q.; Zhou, J. Z.; Xu, X.; Yin, K.; Lou, L. C.; Jiao, M. H.; Zhang, B. W.; Wu, H. J. et al. Multinary alloying for facilitated cation exchange and suppressed defect formation in Kesterite solar cells with above 14% certified efficiency. *Nat. Energy* **2024**, *9*, 1095–1104.

[18] Ma, S. Y.; Li, H. K.; Hong, J.; Wang, H.; Lu, X. S.; Chen, Y.; Sun, L.; Yue, F. Y.; Tomm, J. W.; Chu, J. et al. Origin of band-tail and deep-donor states in Cu_2ZnSnS_4 solar cells and their suppression through Sn-Poor composition. *J. Phys. Chem. Lett.* **2019**, *10*, 7929–7936.

[19] Guo, J. J.; Ao, J. P.; Zhang, Y. A critical review on rational composition engineering in Kesterite photovoltaic devices: Self-regulation and mutual synergy. *J. Mater. Chem. A* **2023**, *11*, 16494–16518.

[20] Li, J. J.; Wang, D. X.; Li, X. L.; Zeng, Y.; Zhang, Y. Cation substitution in earth-abundant Kesterite photovoltaic materials. *Adv. Sci.* **2018**, *5*, 1700744.

[21] Yang, J.; Fu, J. J.; Dong, W. W.; Ren, S.; Zhang, X.; Su, J. Y.; Zhao, C. L.; Wei, M.; Zhao, D. D.; Zhang, Y. G. et al. N-type Ag_2S modified CZTSSe solar cell with lowest $V_{oc,def}$. *Energy Environ. Sci.* **2024**, *17*, 9346–9358.

[22] Wei, H.; Cui, C. C.; Li, Y. M.; Wu, Z. C.; Wei, Y. J.; Han, Y. L.; Han, L.; Lu, B. Y.; Wang, X.; Pang, S. P. et al. Regulating heterogeneous nucleation enabling over 14% efficient Kesterite solar cells. *Small* **2024**, *20*, 2308266.

[23] Dong, L. Z.; Tao, S. Y.; Zhao, M.; Zhuang, D. M.; Wang, Y. F.; Wang, H. P.; Jia, M. Y.; Han, J. S.; Zhu, H. W. Crystallization mechanism and defect passivation of $Cu_2ZnSn(S,Se)_4$ thin film solar cells via *in situ* potassium doping. *J. Mater. Chem. A* **2023**, *11*, 20139–20150.

[24] Liu, J. L.; Wu, X. Y.; Xue, Y.; Liu, S.; Zhu, Z. Y.; Liu, X. S.; Cheng, K.; Du, Z. L. Se as hetero-nucleation seeds reinforcing intermetallic diffusion for improved electrodeposition-processed CZTS solar cells. *Nano Energy* **2024**, *130*, 110183.

[25] Yuan, X. J.; Li, J. J.; Huang, J. L.; Yan, C.; Cui, X.; Sun, K. W.; Cong, J. L.; He, M. R.; Wang, A.; He, G. J. et al. 10.3% efficient green Cd-free Cu_2ZnSnS_4 solar cells enabled by liquid-phase promoted grain growth. *Small* **2022**, *18*, 2204392.

[26] Kim, S. Y.; Son, D. H.; Kim, S. H.; Kim, Y. I.; Kim, S.; Ahn, K.; Yang, K. J.; Kang, J. K.; Kim, D. H. Effect of Cu–Sn–Se liquid phase on grain growth and efficiency of CZTSSe solar cells. *Adv. Energy Mater.* **2020**, *10*, 1903173.

[27] Yu, Q.; Shi, J. J.; Guo, L. B.; Duan, B. W.; Luo, Y. H.; Wu, H. J.; Li, D. M.; Meng, Q. B. Eliminating multi-layer crystallization of $Cu_2ZnSn(S,Se)_4$ absorber by controlling back interface reaction. *Nano Energy* **2020**, *76*, 105042.

[28] Jian, Y.; Xie, T. L.; Han, L. T.; Cao, L.; Wang, L. J.; Zhou, W. H.; Zhou, Z. J.; Kou, D. X.; Meng, Y. N.; Qi, Y. F. et al. Grain growth mechanism of CZTSSe films controlled by the evaporation area of Se. *Sol. RRL* **2023**, *7*, 2300006.

[29] Li, J. J.; Huang, J. L.; Cong, J. L.; Mai, Y. H.; Su, Z. H.; Liang, G. X.; Wang, A.; He, M. R.; Yuan, X. J.; Sun, H. et al. Large-grain spanning monolayer $Cu_2ZnSnSe_4$ thin-film solar cells grown from metal precursor. *Small* **2022**, *18*, 2105044.

[30] Zhou, J. Z.; Xu, X.; Duan, B. W.; Wu, H. J.; Shi, J. J.; Luo, Y. H.; Li, D. M.; Meng, Q. B. Regulating crystal growth via organic lithium salt additive for efficient Kesterite solar cells. *Nano Energy* **2021**, *89*, 106405.

[31] Jian, Y.; Han, L. T.; Kong, X. R.; Xie, T. L.; Kou, D. X.; Zhou, W. H.; Zhou, Z. J.; Yuan, S. J.; Meng, Y. N.; Qi, Y. F. et al. Segmented control of selenization environment for high-quality $Cu_2ZnSn(S,Se)_4$ films toward efficient Kesterite solar cells. *Small Methods* **2024**, *19*, 2400041.

[32] Wang, L. J.; Chu, L. L.; Zhou, Z. J.; Zhou, W. H.; Kou, D. X.; Meng, Y. N.; Qi, Y. F.; Yuan, S. J.; Han, L. T.; Yang, G. et al. Synergistic crystallization modulation and defects passivation in Kesterite via anion-coordinate precursor engineering for efficient solar cells. *Adv. Sci.* **2024**, *11*, 2405016.

[33] Gao, C.; Li, W. B.; Zhou, X. W.; Xu, H. Y.; Zhou, Q.; Gao, H. F.; Qin, S. M.; Gao, Z. R.; Yu, W. Simultaneously improving the morphology and defect properties of CZTSSe film via hybrid grain-growth mechanism. *Sol. Energy Mater. Sol. Cells* **2023**, *251*, 112147.

[34] Zhou, Q.; Li, H.; Wu, T. C.; Liu, Y.; Wang, X. Z.; Li, J. J.; Yu, W.; Gao, C. Improving surface and bulk crystallinities of $Cu_2ZnSn(S,Se)_4$ films simultaneously by finely adjusting the chemical state of S in precursor films. *Appl. Mater. Today* **2025**, *44*, 102707.

[35] Gao, C.; Sun, Y. Z.; Wu, T. C.; Li, H.; Liu, Y.; Zhou, Q.; Gao, Z. R.; Wang, X. Z.; Li, J. J.; Yu, W. Regulating the $NaSe_x$-assisted crystallization of $Cu_2ZnSn(S,Se)_4$ film by modifying the reaction between Na source and Se in co-selenization process. *Sol. Energy Mater. Sol. Cells* **2025**, *292*, 113771.

[36] Zhou, Q.; Sun, Y. L.; Li, H.; Sun, Y. Z.; Zhao, W.; Liang, B. L.; Wang, Y.; Ma, Y. J.; Zhao, L.; Teng, X. Y. et al. Tailoring addition sequence of metal ions in precursor solution drives highly efficient Kesterite solar cells. *Adv. Funct. Mater.* **2024**, *34*, 2313301.

[37] Ding, D. L.; Sun, Y. L.; Li, W. B.; Sun, Y. Z.; Cong, R. D.; Wang, Z. R.; Gao, C.; Yu, W. Efficient window layer modification enabling the remarkable FF and efficiency improvement of Kesterite solar cell. *Chem. Eng. J.* **2024**, *497*, 155050.

[38] Dimitrievska, M.; Fairbrother, A.; Saucedo, E.; Pérez-Rodríguez, A.; Izquierdo-Roca, V. Influence of compositionally induced defects on the vibrational properties of device grade $Cu_2ZnSnSe_4$ absorbers for Kesterite based solar cells. *Appl. Phys. Lett.* **2015**, *106*, 073903.

[39] von Hauff, E. Impedance spectroscopy for emerging photovoltaics. *J. Phys. Chem. C* **2019**, *123*, 11329–11346.

[40] Yan, C.; Huang, J. L.; Sun, K. W.; Johnston, S.; Zhang, Y. F.; Sun, H.; Pu, A. B.; He, M. R.; Liu, F. Y.; Eder, K. et al. Cu_2ZnSnS_4 solar cells with over 10% power conversion efficiency enabled by heterojunction heat treatment. *Nat. Energy* **2018**, *3*, 764–772.

[41] Zhou, J. Z.; Xu, X.; Wu, H. J.; Wang, J. L.; Lou, L. C.; Yin, K.; Gong, Y. C.; Shi, J. J.; Luo, Y. H.; Li, D. M. et al. Control of the phase evolution of Kesterite by tuning of the selenium partial pressure for solar cells with 13.8% certified efficiency. *Nat. Energy* **2023**, *8*, 526–535.

[42] Hages, C. J.; Koeper, M. J.; Miskin, C. K.; Brew, K. W.; Agrawal, R. Controlled grain growth for high performance nanoparticle-based Kesterite solar cells. *Chem. Mater.* **2016**, *28*, 7703–7714.

[43] Abzieher, T.; Schnabel, T.; Hetterich, M.; Powalla, M.; Ahlswede, E. Source and effects of sodium in solution-processed Kesterite solar cells. *Phys. Status Solidi (a)* **2016**, *213*, 1039–1049.

[44] Glazov, V. M.; Pashinkin, A. S.; Fedorov, V. A. Phase equilibria in the Cu–Se system. *Inorg. Mater.* **2000**, *36*, 641–652.

[45] Yoo, H.; Jang, J. S.; Shin, S. W.; Lee, J.; Kim, J.; Kim, D. M.; Lee, I. J.; Lee, B. H.; Park, J.; Kim, J. H. Influence of the reaction pathway on the defect formation in a $Cu_2ZnSnSe_4$ thin film. *ACS Appl. Mater. Interfaces* **2021**, *13*, 13425–13433.

[46] Yang, K. J.; Kim, S.; Sim, J. H.; Son, D. H.; Kim, D. H.; Kim, J.; Jo, W.; Yoo, H.; Kim, J.; Kang, J. K. The alterations of carrier separation in Kesterite solar cells. *Nano Energy* **2018**, *52*, 38–53.

[47] Son, D. H.; Jeon, D. H.; Kim, D. H.; Kang, J. K.; Sung, S. J.; Lee, J.; Lee, T.; Enkhbayar, E.; Kim, J.; Yang, K. J. Identifying the relationships between subsurface absorber defects and the characteristics of Kesterite solar cells. *Carbon Energy* **2023**, *5*, e336.

[48] Wolter, M. H.; Carron, R.; Avancini, E.; Bissig, B.; Weiss, T. P.; Nishiwaki, S.; Feurer, T.; Buecheler, S.; Jackson, P.; Witte, W. et al. How band tail recombination influences the open-circuit voltage of solar cells. *Prog. Photovoltaics* **2022**, *30*, 702–712.

[49] Chantana, J.; Kawano, Y.; Nishimura, T.; Mavlonov, A.; Minemoto, T. Impact of Urbach energy on open-circuit voltage deficit of thin-film solar cells. *Sol. Energy Mater. Sol. Cells* **2020**, *210*, 110502.

[50] Hegedus, S. S.; Shafarman, W. N. Thin-film solar cells: Device measurements and analysis. *Prog. Photovoltaics* **2004**, *12*, 155–176.